Atomically Dispersed Cu–Ni Dual-Metal Sites on g-C 3 N 4 for Synergistic Enhancement of Photocatalytic Hydrogen Evolution

Hafijul Islam, Bhavya Jaksani, Asif Iqbal, Sagar Varangane, Harshini Annadata, Biplab Ghosh, Bidyut Bikash Sarma, Ranjit Thapa, Ujjwal Pal

Atomically Dispersed Cu-Ni Dual-Metal Sites on g-C_3N_4 for Synergistic Enhancement of Photocatalytic Hydrogen Evolution

Hafijul Islam, [a, b] Bhavya Jaksani, [a, b] Asif Iqbal, [c, d] Sagar Varangane, [a, b] Harshini V Annadata, [e] Biplab Ghosh, [e] Bidyut Bikash Sarma, [f] Ranjit Thapa*[c, d] and Ujjwal Pal.* [a, b]

[a]Department of Energy & Environmental Engineering, CSIR-Indian Institute of Chemical Technology, Hyderabad, Telangana 500007, India.

[b]Academy of Scientific and Innovative Research (AcSIR), Ghaziabad 201002, India. Email: upal03@gmail.com; ujjwalpal@iict.res.in

[e]Beamline Development & Application Section, Bhabha Atomic Research Center, Mumbai 400085, India.

[f]Laboratoire de Chimie de Coordination (LCC), CNRS, Université de Toulouse, INPT, UPR 8241,205 route de Narbonne, 31077 Toulouse Cedex 4, France

[c]Department of Physics, SRM University AP, Amaravati 522 240 Andhra Pradesh, India

[d]Centre for Computational and Integrative Sciences, SRM University – AP, Amaravati 522 240, Andhra Pradesh, India. Email: ranjit.t@srmap.edu.in

Abstract:

Single-atom catalysts (SACs) offer a promising strategy to enhance light utilization and charge carrier dynamics in photocatalytic hydrogen evolution. However, the uniform dispersion and stabilization of single-atom active sites remain a significant challenge. Herein, we report the fabrication of atomically dispersed Cu and Ni dual-metal sites anchored on graphitic carbon nitride (CuNi-g-C_3N_4), achieving an outstanding hydrogen evolution rate of 1275 $\mu molg^{-1}h^{-1}$ under visible light irradiation. The synergistic interaction between Cu and Ni bimetallic dual atom catalysts (DACs) modulates the electronic structure of g-C_3N_4, creating active sites and suppressing charge recombination, as confirmed by density functional theory (DFT) calculation. X-ray absorption spectroscopy (XAS) analysis verifies the atomic dispersion of Cu and Ni sites, revealing their interactions with the carbon nitride framework. Photoluminescence (PL) spectroscopy and electrochemical impedance spectroscopy (EIS) further demonstrate enhanced charge separation and reduced recombination in CuNi-g-C_3N_4. The catalyst exhibits excellent stability and maintains its photocatalytic activity over multiple reaction cycles, underscoring the

potential of DACs for sustainable hydrogen production. This study provides new insights into the rational design of dual single-atom catalysts for efficient conversion of solar energy to hydrogen.

Keywords: *g-C_3N_4, dual-single atoms, photocatalysis, water splitting, XAS, DFT.*

1. Introduction

Photocatalytic water splitting offers a sustainable and promising pathway for solar-driven hydrogen production, addressing both the global energy crisis and environmental challenges. The ongoing dependence on fossil fuels like coal and oil not only heightens the risk of energy shortages but also accelerates environmental degradation.[1, 2] By harnessing solar energy, photocatalytic water splitting provides a long-term strategy to mitigate climate change while enabling the production of clean and renewable hydrogen fuel. This technology holds great potential to revolutionize energy systems, paving the way for a greener and more sustainable future.[3-5]

Despite significant advances in the design and modification of photocatalysts, the efficiency of photocatalytic water splitting remains limited by poorly defined charge transfer pathways and a scarcity of active sites. These issues continue to pose major bottlenecks to achieving the performance required for practical applications.[6] Downsizing metal particles to the atomic scale greatly improves metal utilization, with SACs showing remarkable activity in a wide range of reactions. Building on this, DACs often deliver even better performance, thanks to the synergistic interactions between neighbouring metal atoms.[7] Noble-metal-free DACs, valued for their abundance, cost-effectiveness and scalability present a promising route for sustainable applications. Recently, DACs have garnered significant interest for their unique photocatalytic properties and superior atom utilization, paving the way for highly efficient catalytic systems.[8, 9] Compared to SACs, DACs feature higher metal loading and more structurally flexible active sites, enhancing their potential for superior catalytic performance.[10]

Over the past decade, DACs have undergone rapid development, demonstrating enhanced catalytic performance in various key reactions, including CO oxidation,[11] hydrogen evolution reaction,[12] H_2O_2 production,[13] degradation of organic pollutants[14] and chemical synthesis.[15] In contrast to nanoscale cluster catalysts, where some atoms remain inaccessible, every atom in SACs actively participates in the reaction, ensuring maximum atomic efficiency.[16] To stabilize exposed single atoms and prevent aggregation caused by high surface free energy, SACs are strategically anchored onto support materials.[17] Moreover, the strong metal-support interaction enables precise modulation of the coordination environment.[18] Many studies have been conducted on the understanding of the evolution of the SACs on the catalytic activity and

selectivity.[19, 20] Single-atom catalysis a frontier in heterogeneous catalysis offers great promise for both practical applications and advancing fundamental understanding of catalytic processes owing to its highly defined structures, optimized atom utilization and distinctive energetics.[21] According to previous studies, g-C_3N_4 satisfies the necessary criteria due to its stability, nitrogen-rich composition, and cost-effective synthesis.[22] The nitrogen sites of g-C_3N_4 can stably anchor metal ions through six extended electron pairs. Additionally, g-C_3N_4 allows for precise control over its morphology and can be easily exfoliated from the bulk structure to form nanosheets with an increased surface area.[23]

In this study, we developed highly efficient DACs by anchoring Cu and Ni atoms onto g-C_3N_4 through a simple pyrolysis method. The significant enhancement in photocatalytic hydrogen evolution is attributed to the synergistic effect of the Cu-Ni dual sites, which improve charge separation, facilitate electron transfer, and suppress electron-hole recombination. Their strong interaction with the g-C_3N_4 support induces favorable electronic and geometric modifications, introduces additional active sites, and optimizes the adsorption and activation of water molecules, offering a promising strategy for fine-tuning the coordination environment in DAC systems to boost catalytic performance. Experimental results demonstrate that the bimetallic modification effectively enhances the HER, yielding a remarkable H_2 production rate of 1275 $\mu molg^{-1}h^{-1}$ with an apparent quantum efficiency (AQE of 0.83% at 420 nm. Further characterization and theoretical calculations confirm that the incorporation of Cu and Ni dual atomic sites facilitates the transfer of photogenerated electrons, improves charge carrier separation and ultimately enhances H_2 generation from water splitting.

2. Experimental Section

2.1. Chemical Reagents

Melamine (MA, 98%), Cyanuric acid (CA, 98%), Citric acid (CTA, 99.5%), Cu $(NO_3)_2.3H_2O$ (99%), Ni $(NO_3)_2.6H_2O$ (99.99%), Na_2S (98%), Na_2SO_3 (98%), Na_2SO_4 (≥99.0%), Nafion solution and ethanol were purchased from Sigma-Aldrich and used as received without any additional purification.

2.2. Preparation of Photocatalysts:

The atomically dispersed CuNi-g-C_3N_4 catalyst was synthesized via thermal pyrolysis polymerization method. MA (10 mmol) and CA (9.5 mmol) were dissolved separately in 30 mL deionized water and they were stirred at 80 °C until transparent solutions obtained and labelled as A and B respectively. The mixture of CTA (2.5 mmol), Cu $(NO_3)_2.3H_2O$ (0.75 mmol), and Ni $(NO_3)_2·6H_2O$ (0.5 mmol) were dissolved in 10 ml water to form solution C, which was mixed with solution B and further stirred for 10 min. Then this mixture was added into A and stirred for

4 hours at room temperature to form supramolecular precursors. Subsequently, the as-prepared product was purified with water and ethanol and dried under vacuum at 60 °C. Finally, the dried sample was ground into powder and calcined at 600 °C under N_2 gas flow in a tube furnace at a heating rate of 5 °C/min yielding CuNi-CN with a 3:2 Cu/Ni molar ratio and named as Cu_3Ni_2-CN. Preparation of Cu-CN and Ni-CN followed the same procedure, with appropriate metal precursors. CN was prepared similarly without any metal precursors. In the following discussion Cu_3Ni_2-CN is referred as CuNi-CN.

2.3. Photocatalytic Experiment

The photocatalysis experiment took place in a nitrogen atmosphere inside a quartz long-necked round-bottom flask, securely sealed with a rubber septum. To prepare the reaction mixture, 20 mg of the catalyst was dispersed in 50 mL of an aqueous solution containing 0.25 M Na_2S and 0.35 M Na_2SO_3 using ultrasonication. To ensure an inert environment, the system was first evacuated for 15 minutes and then purged with nitrogen for 30 minutes. The reaction was then illuminated using a 420 W Xe lamp equipped with a 420 nm cutoff filter ($\lambda > 420$ nm) to ensure visible-light irradiation. For AQE measurements, monochromatic light at 420 nm was used, with continuous stirring to keep the catalyst evenly dispersed. The gases produced during the reaction were carefully sampled using a 100 μL airtight syringe and analyzed with a Perkin Elmer gas chromatograph (Clarus 590) with a thermal conductivity detector (TCD).

3. Result and discussion:

Atomically dispersed bimetallic Cu–Ni dual sites on graphitic carbon nitride were synthesized via a thermal pyrolysis polymerization method carried out under a nitrogen atmosphere. This inert environment was used to prevent the oxidation of both the carbon nitride framework and the incorporated metal species. The synthesis employed supramolecular precursors, as illustrated in Figure 1a. The X-ray diffraction (XRD) patterns (Figure 1b and Figure S1) display characteristic peaks at 13.3°and 27.5°, associated with the (100) and (002) planes of CN, respectively. The observed diffraction spectrum closely matches the standard JCPDS card no. 87-1526.[24] For Ni-CN, Cu-CN, and CuNi-CN, only the peak at 27.5° was observed, which indicates that the incorporation of Ni and Cu alters the stacking configuration of the tri-s-triazine units within the CN structure.[25] Importantly, no diffraction peaks specific to Cu or Ni metals were observed, implying their even distribution across the CN matrix. Inductively coupled plasma optical emission spectroscopy (ICP-OES) was used to determine the weight percentages of Cu and Ni in CuNi-CN, which are 0.49 wt% and 0.32 wt%, respectively in CuNi-CN samples as indicated in Table S1 and the percentage of C, H, N determined by CHNS analysis as given in Table S2. The FT-IR spectra of CuNi-CN (Figure 1c) reveal characteristic structural features of

CN. The C–N and C=N stretching vibrations appear in the range of 1200–1700 cm^{-1}, corresponding to the aromatic C–N and C=N bonds within the heptazine or tri-s-triazine units the fundamental building blocks of CN. A distinct peak near 800 cm^{-1} is attributed to the breathing mode of the triazine rings, confirming the preservation of the heptazine structure. These findings suggest that CuNi-CN retains the graphitic phase structure of CN. Additionally, a broad band observed between 3300–3500 cm^{-1} is associated with N–H or O–H stretching vibrations, likely originating from surface functional groups of CN or adsorbed moisture.[26, 27] From the magnified spectra as presented in Figure S2, the C-N stretching in Cu-CN, Ni-CN and CuNi-CN is blue-shifted compared to the CN. This indicates there is Cu and Ni interaction impacting the N environment.

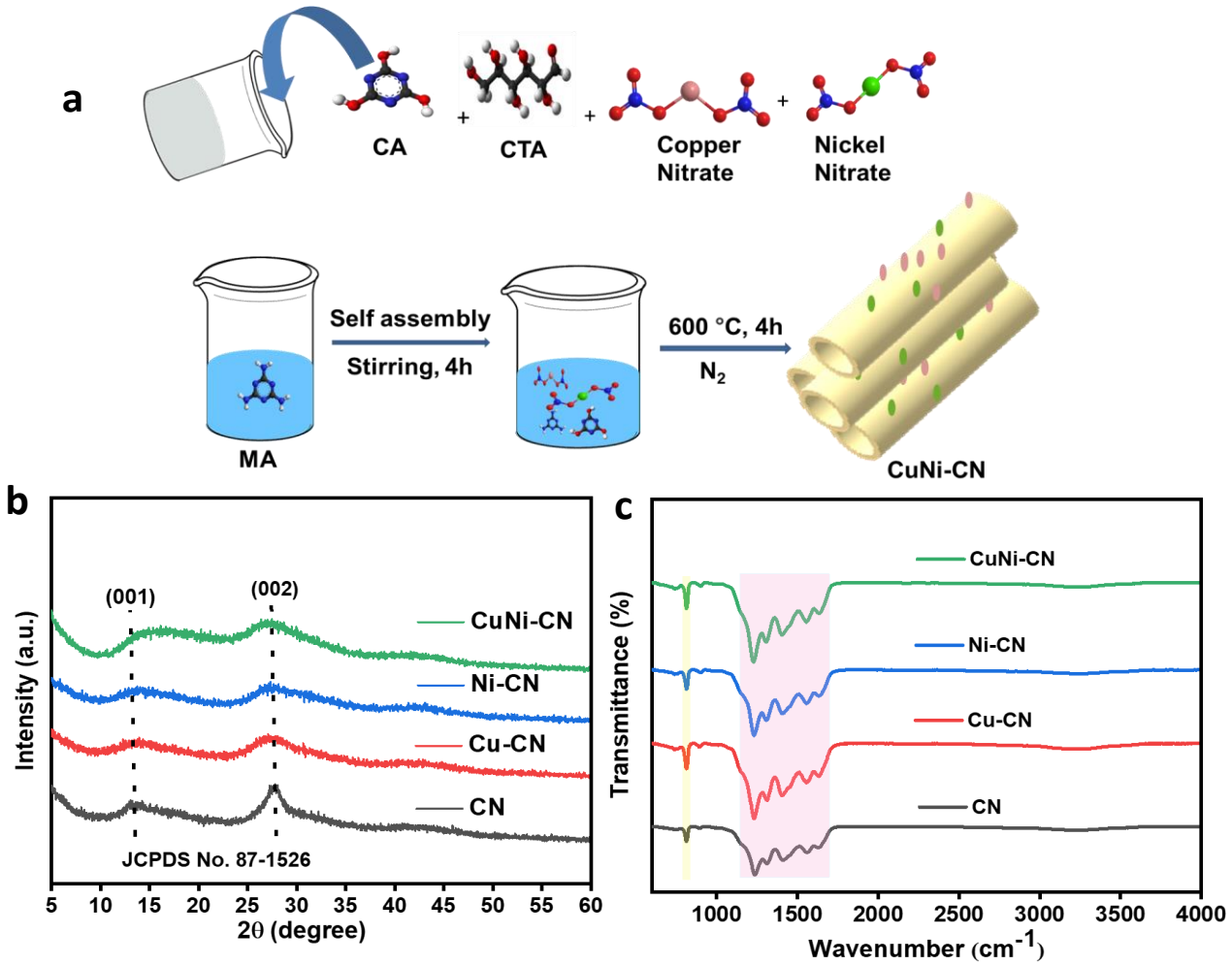

Figure 1. (a) The schematic illustration of synthesizing the CuNi-CN (b) XRD patterns and (c) FTIR spectra of CN, Cu-CN, Ni-CN and CuNi-CN respectively.

The morphology of CuNi-CN was further investigated using transmission electron microscopy (TEM) and high-angle annular dark field scanning transmission electron microscopy (HAADF-STEM). As shown in Figure 2a, the representative TEM image of CuNi-CN displays intertwined tubular structures, preserving the same morphological characteristics as pristine CN (Figure S3).

Notably, no Cu or Ni based nanoparticles or nanoclusters are observed on the surface of CuNi-CN. The selected area electron diffraction (SAED) pattern (inset in Figure 2a) confirms the absence of any prominent crystalline phase in CuNi-CN. Furthermore, the HAADF-STEM image in Figure 2b-c reveals numerous bright dots, highlighted by red in Figure 2c circles, indicating the presence of individually isolated and uniformly dispersed Cu and Ni single atoms within the CN matrix of CuNi-CN. The HAADF-STEM images of Cu-CN and Ni-CN are provided in Figure S4. Furthermore, energy-dispersive X-ray (EDX) elemental mapping confirmed the uniform dispersion of Cu and Ni elements within the CN matrix. The successful loading of Cu and Ni dual sites in CuNi-CN was corroborated through HAADF-STEM-EDX mapping, as shown in Figure 2d-h.

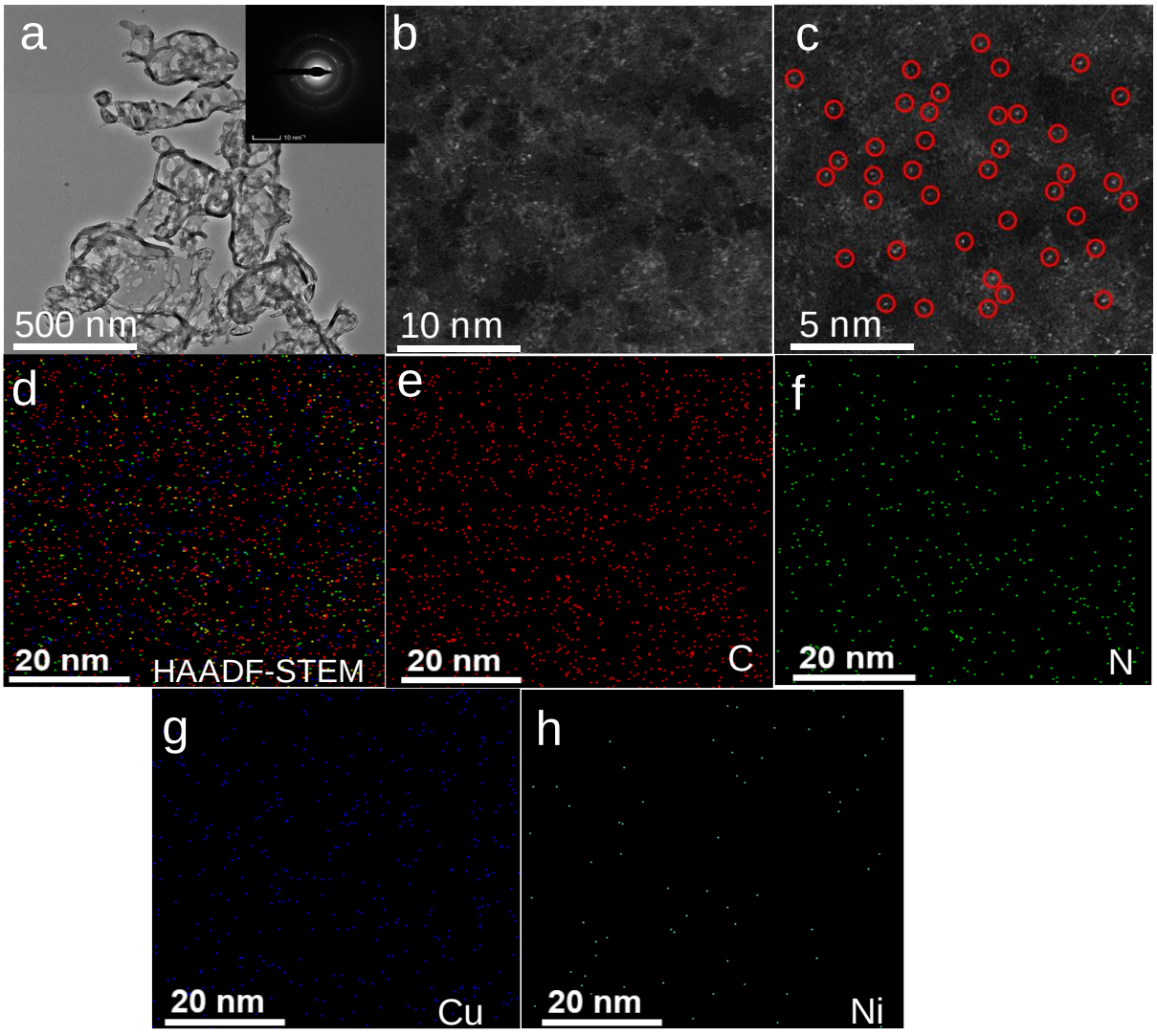

Figure 2. (a) TEM images of CuNi-CN (b, c) HAADF-STEM images of CuNi-CN (d) HAADF-STEM-EDX elemental mapping of CuNi-CN and the corresponding elemental mappings of (e) C, (f) N (g) Cu (h) Ni

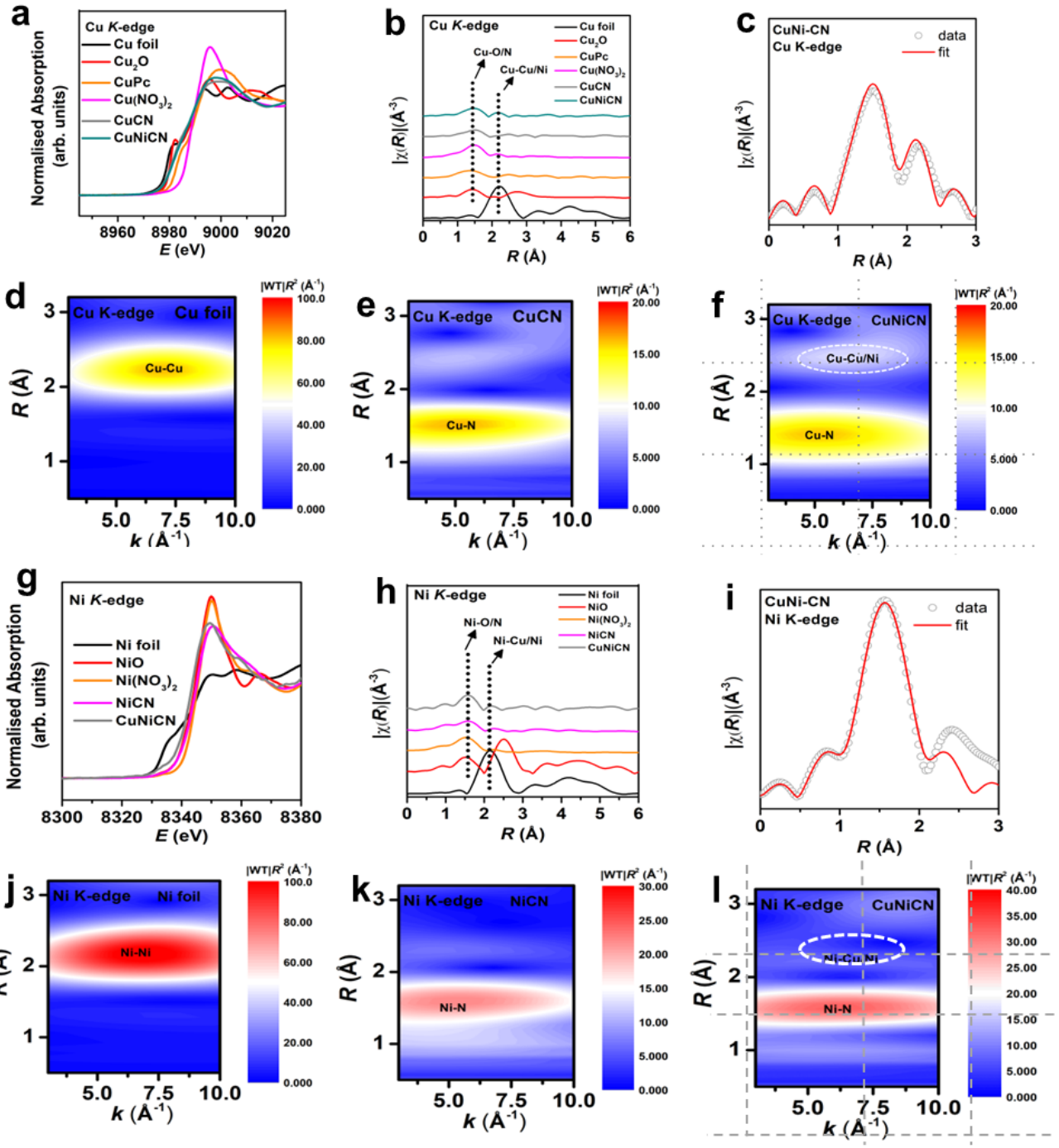

Figure.3 (a) Cu *K*-edge XANES spectra of the Cu foil, Cu_2O, CuPc, Cu $(NO_3)_2$, Cu-CN and CuNi-CN (b) k^2-weighted Fourier-transform Cu *K*-edge EXAFS spectra of the samples (c) Cu *K*-edge EXAFS fitting curves of the CuNi-CN catalyst in the R space. Wavelet-transformed k^2-weighted EXAFS spectra of d) the Cu foil, e) Cu-CN and f) CuNi-CN. (g) Ni *K*-edge XANES spectra of the Ni foil, NiO, Ni $(NO_3)_2$, Cu-CN and CuNi-CN. (h) k^2-weighted Fourier-transform Ni *K*-edge EXAFS spectra of the samples (i) Ni *K*-edge EXAFS fitting curves of the CuNi-CN catalyst in the R space. Wavelet-transformed k^2-weighted EXAFS spectra of (j) the Ni foil, (k) Ni-CN and (l) CuNi-CN.

The structural and electronic properties of Cu and Ni sites are characterized using X-ray absorption near-edge spectroscopy (XANES) and Fourier transform extended X-ray absorption Fine Structure (FT-EXAFS) which has been reported to be vital tool for SACs.[28] Figure 3a illustrates the Cu K-edge XANES spectra of Cu-CN and CuNi-CN. The edge positions of both samples closely resemble those of Cu foil, CuPc (Copper Phthalocyanine) and Cu_2O. The white line intensity at the Cu K-edge shows that it resembles closely to CuPc which infers that Cu is positively charged in these catalysts. This observation is consistent with the XPS analysis as shown in Figure 4d. The k^2-weighted FT-EXAFS of Cu-CN, CuNi-CN are shown in Figure 3b compared with Cu foil, Cu_2O, CuPc and Cu $(NO_3)_2$ only shows the main peak at 1.45 Å, which can be attributed to the Cu-N coordination. No Cu-Cu coordination peak (2.18 Å) is observed, indicating that there are no Cu nanoparticles in the Cu-CN sample. However, a small peak is observed for CuNi-CN which is due to Cu-Ni or Cu-Cu interaction. To further confirm the presence of Cu−N and Cu−Cu/Ni bonds, Morlet wavelet transformations (WT) were performed at the Cu K-edge.[29] As shown in Figure 3c and Figure S5, the WT of Cu foil exhibits a single lobe at 2.1 Å, while the Cu−N bond in Cu−CN is presented in Figure 3e. Figure 3f illustrates that the Cu−N bond is preserved and the Cu−Cu/Ni bond is formed as per the lobe at approximately 2.5 Å. EXAFS fitting was conducted to determine the structural parameters and quantitative chemical configurations of the Cu atoms, with the fitted curves presented in Figure S7 and Figure 3c for Cu-CN and CuNi-CN respectively. The coordination number of the central Cu atom was approximately 3, and the average bond lengths of Cu-N/C are listed in Table S3.

To further confirm the valence states and coordination structure of the Ni single atom in Ni-CN and CuNi-CN, XANES and EXAFS spectroscopy at the Ni K-edge were conducted. The Ni K-edge XANES spectrum of Ni-CN and CuNi-CN catalysts were compared with that of standard samples of NiO and Ni $(NO_3)_2$ (Figure 3g). The white line intensity at the Ni K-edge shows features which is in between Ni (0) and Ni (2+). Therefore, the Ni can be assumed to be slightly higher than +1 oxidation state. In the FT-EXAFS spectrum (Figure 3h), NiO and Ni $(NO_3)_2$ exhibit a primary peak at 1.56 Å, corresponding to the scattering of Ni-N coordination. Notably, no Ni-Ni coordination peak at 2.12 Å was detected, confirming the absence of Ni nanoparticles in the Ni-CN sample. However, a small peak is observed for CuNi-CN which is due to Cu-Ni/Cu interaction. To further confirm the presence of Ni−N and Ni−Cu/Ni bonds, WT were performed at the Ni K-edge. As shown in Figure 3j, the WT spectrum of Ni foil exhibits a single lobe at 2.1 Å while the Ni−N bond in Ni−CN is presented in Figure 3k and Figure S6. Figure 3l illustrates that the Ni−N bond is preserved and the Ni−Cu/Ni bond is formed as per the lobe at approximately 2.2 Å. EXAFS fitting was employed to elucidate the structural parameters

and quantitative chemical configurations of the Ni atoms, with the corresponding fitted curves depicted in Figure S8 and Figure 3i for Ni-CN and CuNi-CN, respectively. The central Ni atom has a coordination number of 4 was found to be the best to fit the EXAFS curve with an average Ni–N_2C_2 bond length of 2.07 Å in Ni-CN. The local atomic structure model of the Ni single atom in CuNi-CN is detailed in Table S4.

Additionally, X-ray photoelectron spectroscopy (XPS) confirmed the presence of C, N and Cu, aligning with EDS analysis (Figure 4a). The high-resolution C 1s spectrum of CuNi-CN (Figure 4b) shows two distinct peaks at 284.9 eV and 288.2 eV, attributed to graphitic carbon (C–C bonds) and sp^2-hybridized carbon (N–C=N) respectively.[30] The N 1s spectrum of CuNi-CN (Figure 4c) exhibits peaks centered at 398.4 eV, 400.6 eV, and 403.6 eV, corresponding to C–N=C bonds, tertiary nitrogen in N-$(C)_3$ groups and C–N–H functional groups, respectively. Notably, the high concentration of pyridinic nitrogen provides favorable coordination sites for Cu–N and Ni–N interactions.[31] The high-resolution Cu 2p XPS spectrum shows two primary peaks at 932.0 eV and 951.8 eV, corresponding to Cu $2p_{3/2}$ and Cu $2p_{1/2}$, respectively. The lack of shake-up satellite features indicates that the Cu species are present in either the Cu^0 or Cu^{+1} oxidation state (Figure 4d).[32] It is important to note that due to low loading of Ni atom in CuNi-CN photocatalyst Ni peak in XPS was not detected.[12, 33]

The UV-visible absorbance spectra of all samples were measured across the wavelength range of 350 to 800 nm, as shown in Figure 4e. The absorption edge of CN appeared in the visible region, enabling its excitation under visible-light irradiation. The UV-vis diffuse reflectance spectra reveal that CuNi-CN significantly enhanced absorption intensities in the wavelength range of 350-700 nm compared to Cu-CN, Ni-CN and CN. Notably, the absorption edges of CN are observed at around 430 nm. The incorporation of Ni, Cu, and bimetallic Ni–Cu single sites into g-C_3N_4 (forming Ni-CN, Cu-CN, and CuNi-CN) results in a slight red-shift of the optical absorption edge, thereby enhancing visible light-harvesting capabilities. This improvement in optical properties is attributed to the synergistic electronic interactions between the metal atoms and the g-C_3N_4 matrix. This aligns with the maximum observed H_2 evolution activity of CuNi-CN. The bandgap energies (E_g) of CN, Cu-CN, Ni-CN, and CuNi-CN were calculated using the Kubelka-Munk function from their optical absorption spectra (Figure 4f), yielding values of 2.70 eV, 2.60 eV, 2.63 eV, and 2.52 eV respectively. The reduced band gap of CuNi-CN enhances light absorption efficiency, significantly boosting its light utilization capacity. PL analysis was conducted to assess the charge recombination dynamics of the catalysts. As shown in Figure 4g, the PL spectrum of pristine CN displays a prominent emission peak at 463 nm corresponding to the inter-band recombination of photogenerated electron-hole pairs. Upon the incorporation of

CuNi DACs, the PL intensity significantly decreases, indicating a reduction in electron-hole recombination. Among all the samples, CuNi-CN exhibits the weakest PL emission, suggesting superior charge separation efficiency. This observation is consistent with the enhanced photocatalytic performance of CuNi-CN. To explore the impact of single atoms on bimetallic synergistic interactions, time-resolved photoluminescence (TRPL) spectroscopy was conducted on the photocatalysts. The average PL lifetime of CuNi-CN was measured at 0.63 ns, longest among the samples CN (0.38 ns), Cu-CN (0.61 ns) and Ni-CN (0.50 ns). The relative contribution and characteristic decay times of each component along with photoluminescence lifetime are tabulated in Table S5. This brief lifetime is indicative of rapid photoinduced charge separation within CuNi-CN and thus resulted in significantly improved charge carrier separation and transport kinetics within the CuNi-CN photocatalyst, leading to enhanced photocatalytic activity Figure 4h.

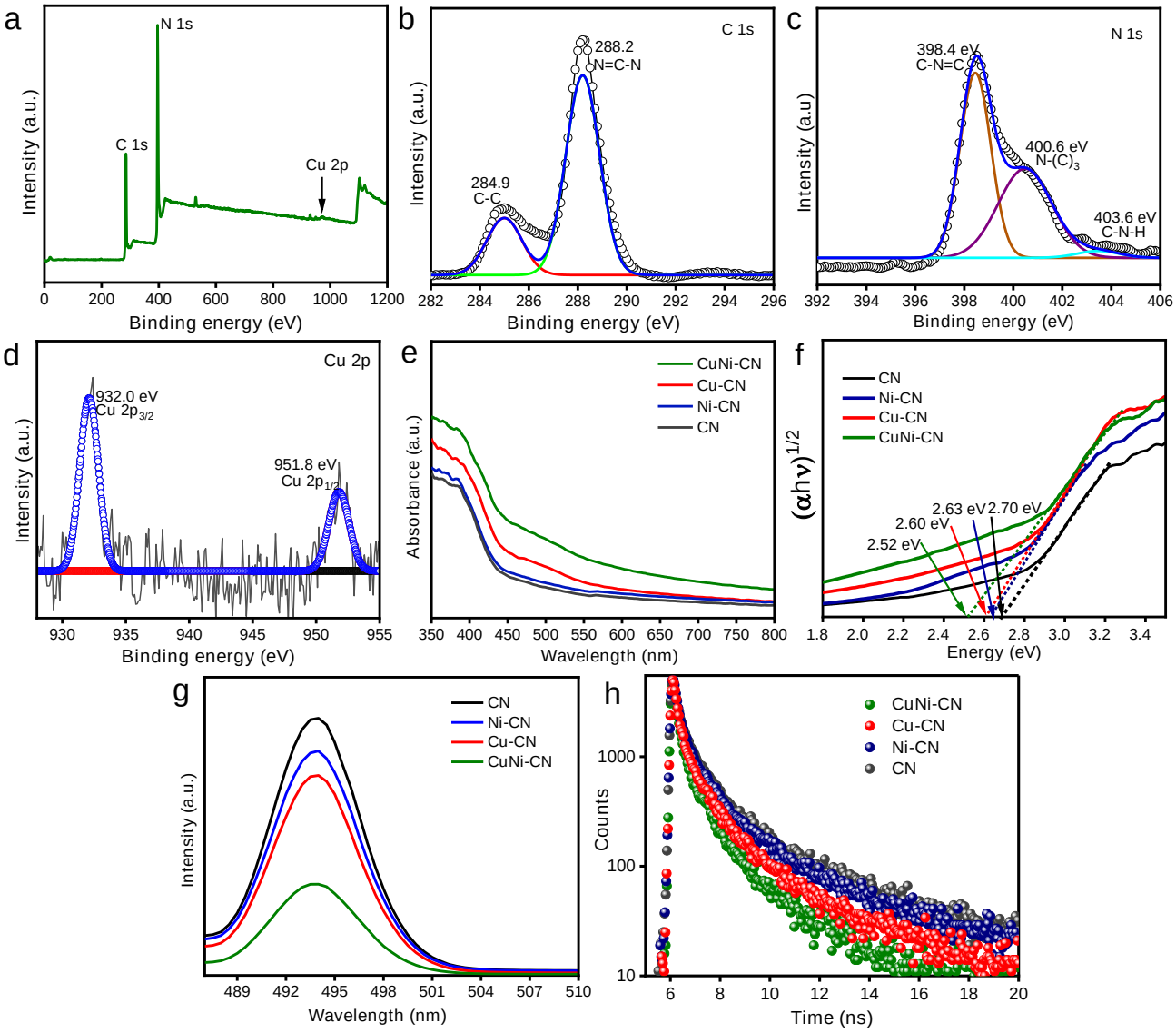

Figure 4. (a) XPS full survey spectra (b) High-resolution XPS spectra of C 1s (c) N 1s (d) Cu 2p of CuNi-CN (e) UV–visible absorbance spectra, (f) Tauc plots, (g) PL spectra and (h) time-resolved PL spectra of CN, Cu-CN, Ni-CN, and CuNi-CN.

3.1. Experimental Measurements of Photocatalytic H_2 Production

In the study on photocatalytic hydrogen evolution reaction (HER) under visible light in aqueous solution, a series of photocatalysts- Cu_3Ni_2-CN, Cu_2Ni_1-CN, Cu_1Ni_2-CN, Cu_1Ni_1-CN, Cu-CN, Ni-CN, and pristine CN were evaluated. Pristine CN exhibited low hydrogen evolution activity (275 $\mu molg^{-1}h^{-1}$), primarily due to the rapid recombination of photogenerated electron-hole pairs. The introduction of SACs significantly improved the photocatalytic performance. Among the monometallic systems, Cu-CN demonstrated better activity than Ni-CN, indicating more effective separation of photoinduced charge carriers, with Cu acting as an efficient electron reservoir. While Cu facilitates charge separation by capturing electrons, Ni contributes by tuning the electronic structure and offering additional active sites for proton adsorption and reduction. Fine-tuning the Cu-to-Ni molar ratio in the bimetallic CuNi-CN catalysts further boosted activity, with Cu_3Ni_2-CN achieving the highest hydrogen evolution rate of 1275 $\mu molg^{-1}h^{-1}$.

This performance improvement is attributed to the synergistic effect between Cu and Ni dual sites, which enhances the transfer of photoinduced electrons to Cu_3Ni_2-CN. The hydrogen production rate of the photocatalysts is shown in Figure 5a and Figure 5b displays the average hydrogen production over 4 hours. Cu_3Ni_2-CN achieved a maximum yield of 5100 $\mu molg^{-1}$ in 4 hours, which is over 4.63 times greater than bare CN. The HER performance of the photocatalysts is summarized in the following order: Cu_3Ni_2-CN > Cu_2Ni_1-CN > Cu_1Ni_2-CN > Cu_1Ni_1-CN > Cu-CN > Ni-CN > CN. A controlled reaction was performed to confirm the hydrogen evolution in the absence of light and catalyst under the same reaction condition. These reactions advocated that HER is possible only when light and catalyst are incorporated into the reaction procedure. Additionally, hydrogen evolution experiments conducted under identical conditions over four consecutive cycles demonstrated consistent H_2 production rates without noticeable activity degradation, confirming the exceptional stability of Cu_3Ni_2-CN (Figure 5c). It is well known that a catalyst's reliability and stability are important factors in its application. The Cu_3Ni_2-CN photocatalyst exhibited remarkable stability and durability during photocatalytic hydrogen evolution. Post-reaction XRD and TEM analyses revealed no significant changes in the catalyst's composition, indicating its structural integrity (Figure S9 and Figure S10). The AQY of the as-prepared photocatalysts was calculated based on their photocatalytic H_2 production performance. Figure S11 presents the AQE values for all catalysts, following the trend: Cu_3Ni_2-CN > Cu_2Ni_1-CN > Cu_1Ni_2-CN > Cu_1Ni_1-CN > Cu-CN > Ni-CN > CN. These

computed AQY values are in excellent agreement with the observed H_2 production results, further confirming the enhanced activity of CuNi bimetallic dual site on CN.

3.2. Photoelectrochemical analyses.

The incorporation of Cu and Ni SACs markedly enhances the photocurrent intensity, indicating the superior ability of CuNi DACs to facilitate charge separation. As shown in Figure 5d, the modification of CN with CuNi DACs further amplifies the photocurrent response. This result underscores the crucial role of CuNi dual sites as active centers, boosting reactant adsorption and serving as efficient electron mediators to promote charge separation compared to Cu-CN, Ni-CN and CN. Additionally, EIS provides valuable insights into the kinetics of charge transfer processes in CuNi-CN, Cu-CN, Ni-CN and CN. Notably, smaller semicircle in the Nyquist plots indicates a faster electron transfer rate within the catalyst.[34] As shown in figure 5e the Nyquist plot radii demonstrate that the presence of CuNi sites enhances electrical conductivity and reduces charge transfer resistance. The distinctive coordination environment of CuNi dual sites facilitates efficient electron transfer from CN to the atomic centres, enabling ultrafast electron hopping. This phenomenon is corroborated with the PL observations. A linear sweep voltammetry (LSV) experiment revealed that the current density of CuNi-CN is significantly higher than that of CN photocatalysts (Figure 5f). This enhancement in current density is attributed to the effective charge separation achieved through the optimal integration of CuNi dual sites into CN. These results demonstrate that incorporation of CuNi in CN significantly boosts its photocatalytic performance.

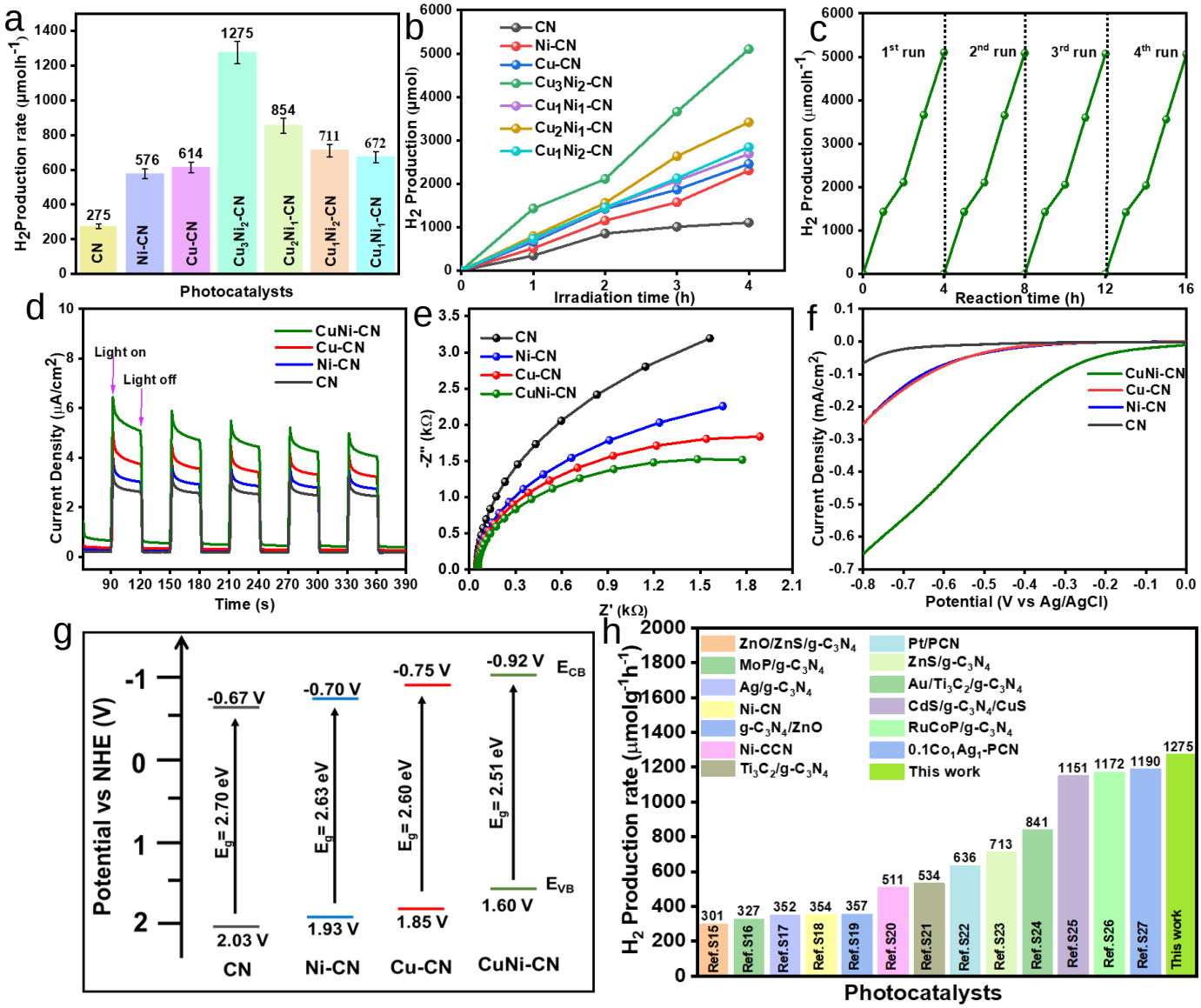

Figure.5 (a) Rate of photocatalytic H_2 production of different catalysts in aqueous solution of Na_2S and Na_2SO_3 in 4h (b) Photocatalytic H_2 production yield (c) recyclability test of the CuNi-CN photocatalyst up to four recurring cycles (d) The photoelectrochemical responses CN, Ni-CN, Cu-CN and CuNi-CN under visible light illumination (e) Electrochemical impedance spectroscopy (EIS) for CN, Ni-CN, Cu-CN and CuNi-CN (f) Linear sweep voltammetry LSV of CuNi-CN, Cu-CN, Ni-CN and CN sample (g) Position of VB and CB of CN, Ni-CN, Cu-CN and CuNi-CN (h) Comparison of photocatalytic HER with other work and this work.

Furthermore, the Mott-Schottky analysis is employed to determine the flat-band potentials (E_{fb}) of the synthesized samples. The flat-band potential is calculated using the following equation.[35]

$$\frac{1}{C^2} = \frac{2}{q\,\epsilon\,\epsilon_0\,N_d}\,E - E_{fb} - \frac{k_b T}{q}$$

Where, E = applied potential, C = space charge capacitance, ϵ = dielectric constant, ϵ_0 =

dielectric constant in vacuum, N_d = donor densities, k_b = Boltzmann constant, T = absolute temperature, and q = electronic charge. The E_{fb} of the examined composites is shown by the crossings of the tangent in the Mott-Schottky plots (Figure S13). The E_{fb} of CN, Ni-CN, Cu-CN, and CuNi-CN are determined to be -0.77 V, -0.80 V, -0.85 V and -1.02 V versus Ag/AgCl at pH 7, corresponding to -0.57 V, -0.60 V, -0.65 V and -0.82 V versus the normal hydrogen electrode (NHE) at the same pH. In the case of n-type semiconductors, the conduction band edge (E_{CB}) is generally positioned approximately 0.1 V more negative than the flat band potential.[12] Therefore, the conduction band potentials of CN, Ni-CN, Cu-CN and CuNi-CN are calculated to be -0.67 V, -0.70 V, -0.75 V and -0.92 V versus NHE at pH 7 respectively and their respective E_{VB} and E_{CB} is given in Figure 5g.

4. The Photocatalytic Mechanism for HER

Based on the findings from both photocatalytic and electrocatalytic studies, we propose an electron transfer pathway and provide mechanistic insights into the water-splitting reaction, as depicted in Figure 6. Upon exposure to light, the CuNi-CN photocatalyst generates e^--h^+ pairs. The photogenerated holes are promptly captured by the sulfide shuttle (S^{2-}/SO_3^{2-}), while the electrons are directed to the conduction band of the semiconductor. Mott-Schottky analysis at the semiconductor interface demonstrates effective electron migration from the conduction band of CN to the atomic Cu and Ni enhancing proton reduction. At the same time, valence band holes are captured by the S^{2-}/SO_3^{2-} shuttle, effectively minimizing the recombination of electron-hole pairs. The addition of Cu and Ni to CN improves light absorption, increases active sites for proton reduction, and enhances photocatalytic performance in water splitting. Sacrificial donors, such as sulfides and sulfites, well-established hole scavenger pair known for its high efficiency and minimal backward reaction in photocatalytic hydrogen evolution studies. The S^{2-}/SO_3^{2-} redox shuttle is particularly effective due to the fast kinetics of hole quenching and the formation of stable oxidation products like thiosulfate ($S_2O_3^{2-}$) and sulfate (SO_4^{2-}), which are less prone to reduction under our experimental conditions.[5,45]

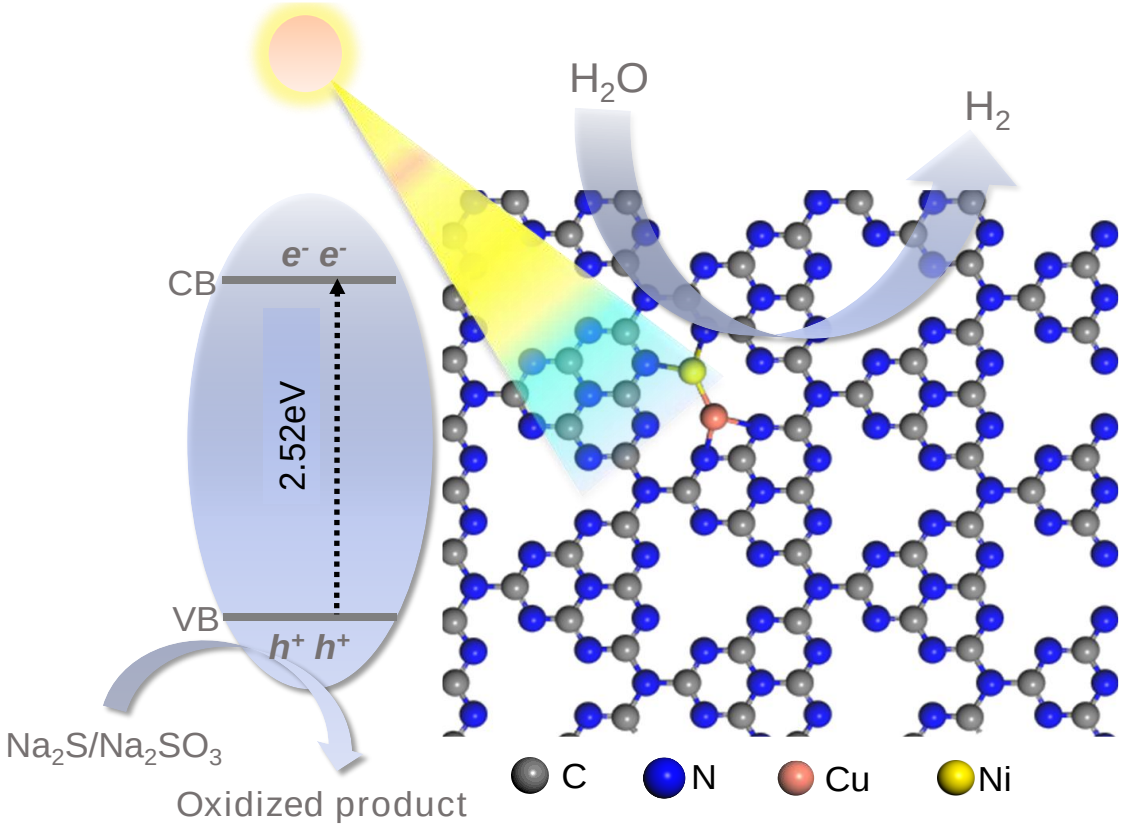

Figure 6. Plausible mechanism of photocatalytic hydrogen evolution through CuNi-CN**.**

Sacrificial sulphate ions contribute to the oxidation process on the VB of CuNi-CN, alongside H^+ ions, leading to the formation of pyrosulphates in the presence of H_2O, as described in Eq. (1). According to Eqs. (2)-(4), additional intermediates, such as dithionate and peroxydisulfide ions, are generated through the direct interaction of holes in the oxidation of sulphate ions to sulphide ions. Meanwhile, the H^+ ions produced or adsorbed at catalytic sites undergo reduction via CB electrons, resulting in H_2 formation Eq. (6). The proposed mechanism for photolytic hydrogen generation using the Na_2S and Na_2SO_3 shuttle is outlined below.

Reaction mechanism:

$$CuNi - CN + h\nu = e^- + h^+ \quad (1)$$

Oxidation reaction at the VB,

$$SO_4^{2-} + H_2O + 2h^+ \rightarrow SO_5^- + 2H^+ \quad (2)$$

$$2SO_4^{2-} + 2h^+ \rightarrow S_2O_8^{2-} \quad (3)$$

$$2S^{2-} + 2h^+ \rightarrow S_2^{2-} \quad (4)$$

$$S^{2-} + SO_4^{2-} \rightarrow S_2O_4^{2-} + S^{2-} \quad (5)$$

Reduction reaction at the CB,

$$2H^+ + 2e^- \rightarrow H_2 \quad (6)$$

5. Theoretical study

In recent days, g-C_3N_4 is well known for producing hydrogen.[36] In this analysis, we have possible boosting of HER activity by introducing Cu and Ni atoms as the active sites for HER.[37, 38] We have compared the change in free energy during hydrogen adsorption on the model structures are to comment on the possible boosting of HER activity. To understand how the dual atoms are boosting the HER than its single atom counterparts, we have compared three model structures (i) M_1 (Cu@g-C_3N_4), (ii) M_2 (Ni@g-C_3N_4) (iii) M_3 (Cu-Ni@g-C_3N_4) (Figure7). The analysis of the HER study is summarized in the Figure 7b. This investigation finds all the model structures can be utilized for HER. Moreover, the G_H value reduces from $|G_H|$ = 0.23 eV in M_1, to $|G_H|$ = 0.28 eV in M_2, and finally to $|G_H|$ = 0.17 eV for Cu site and 0.22 eV for Ni site in M_3 model structure. Later, to understand the possible reason for improved HER activity in comparison to the g-C_3N_4, we have analysed the density of states (DOS) (Figure 7c) projector density of states (PDOS) for the materials as shown in Figure 7d and 7e. This analysis finds that, the enhancement of density of states of the electrons around the fermi level may be the possible reason for the upgradation of HER on the material.

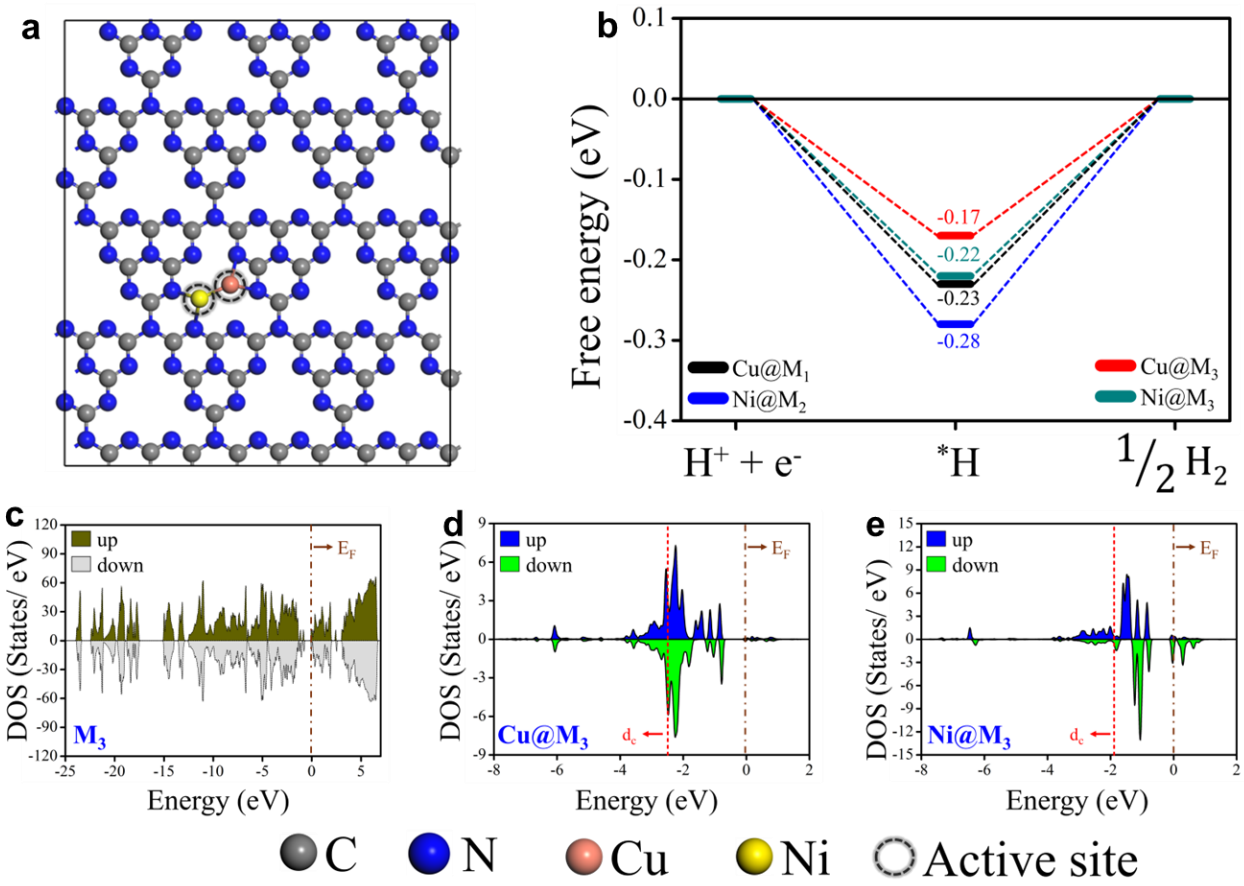

Figure 7. (a) Top view of model structure of Cu-Ni dual atom doped g-C_3N_4 (M_3); (b) free energy profile for hydrogen evolution reaction (HER) on the three model structures with Cu and Ni active site; (c) density of states (DOS) of M_3; Projected density of states (PDOS) of (d) Cu@M_3 and (e) Ni@M_3. Here, black, blue, tan and yellow coloured sphere respectively indicates carbon, nitrogen, copper and nickel atom and the hollow sphere implies active site.

Later, we have analysed of d-band centre (d_c) on the three models to possibly explain the underlying mechanism for the improvement of HER. This analysis identifies of d_c from -1.17 eV on Cu@M_1 (closer to fermi level) to -2.49 (far from fermi level) for Cu@M_3 (Table 1). This shifting of d_c far from fermi level leads to the weakening of the adsorption of hydrogen on Cu@M_3 than Cu@M_1 resulting the reduction of $|G_H|$. Similarly, the switching of d_c from -1.65 eV in Ni@M_2 to -1.89 eV in Ni@M_3 resulting the lowering of $|G_H|$ for similar reason (Table 1). The metal atoms plays important role to facilitate the charge transfer and also prohibits the agglomeration by adding stability to the system.[39] Further, the variation of available charges and the d_c with the alteration of relative position of the active sites hints out the possible synergistic effect on the active sites.[40] Further, the available charges and with the alteration of relative

position of the d_c of the active sites indicate the possible synergistic effect.[41] This effect finally improves the HER activity by refining the overpotential $|G_H|$, indicating Cu and Ni acts as dual active sites on g-C_3N_4 which is consistent with the previous reports and also the experimental observations.[42]

Model	Site	d_c (eV)	Charge on active site (|e|)	$\|G_H\|$ (eV)
Cu@g-C_3N_4 (M_1)	Cu	-1.17	10.26	0.23
Ni@g-C_3N_4 (M_2)	Ni	-1.65	9.23	0.28
Cu-Ni@g-C_3N_4 (M_3)	Cu	-2.49	10.52	0.17
	Ni	-1.49	9.55	0.22
g-C_3N_4 with O group[42]	C/N	NA	--	> 1.00
Ag@g-C_3N_4[43]	Ag	NA	--	0.48
AgPt@g-C_3N_4[44]	Ag	NA	--	0.32

Table 1: Summary of charge on the active site, occupancy, d-band centre (d_c) and free energy change $|G_H|$ of three model structure M_1, M_2 and M_3 of Cu doped, Ni doped and Cu-Ni dual atom doped g-C_3N_4 catalysts for investigating the hydrogen evolution reaction (HER) obtained in this work ($^{\#}$ represents the results of this work) with the previous reports.

5. Conclusion

The synthesis of highly dispersed Cu-Ni dual sites on g-C_3N_4 surfaces was achieved through a solvothermal process followed by pyrolysis. The resulting Cu_3Ni_2-CN photocatalyst exhibited a significantly enhanced H_2 production rate of 1275 $\mu molg^{-1}h^{-1}$, with an AQE of 0.83%. This remarkable improvement in photocatalytic activity, compared to its single-site counterparts, is attributed to the synergistic effect of the Cu-Ni dual sites and their distinct coordination environment with CN. The dual-site configuration modulates the charge density of the Cu-Ni centers as found by DFT calculation, facilitating efficient electron transfer to the metal sites during the HER. Unlike single-atom catalysts, which often exhibit limited activity, the Cu-Ni dual sites not only reduce the free energy barrier for hydrogen evolution, but also enhance the local electron density around the metal centers, promoting more efficient catalytic processes. This study provides new insights into the rational design of photocatalysts with atomic precision, highlighting the importance of dual-metal active sites and their coordination

environments. It further underscores the potential of dual-site single-atom catalysts for advancing solar energy conversion technologies.

Supporting Information

Detailed information on material characterization, computational methods, photoelectrochemical investigations, X-ray absorption spectroscopy (XAS), apparent quantum efficiency (AQE) calculations for H_2 production, TEM and HAADF-STEM imaging, Mott-Schottky analysis, ICP-MS measurements, AQE values of the as-prepared photocatalysts, XRD patterns, time-resolved photoluminescence (TRPL) lifetime analysis, CHNS elemental analysis, and a comparative study of H_2 production rates among different photocatalysts is provided in the Supporting Information

Acknowledgments

This work was supported by MoES, New Delhi (Project no: GAP-1086) and HPCL (Project no: CLP-0138/HPCL). H. Islam and B. Jaksani acknowledge AcSIR for Ph. D enrollment and H. Islam thanks UGC. A. Iqbal and R. Thapa sincerely acknowledge NSM for access to PARAM Rudra at IUAC, Delhi, for computational work. R. Thapa also thanks SERB, India (Grant no: CRG/2022/005423). We would like to thank Vincent Colliere from LCC-CNRS for performing high-resolution microscopy measurement. CSIR-IICT Communication no: IICT/Pubs./2025/089.

Notes

The authors declare no competing financial interest.

References.

1. Chanda, N.; Biswas, B.; Islam, H.; Abraham, B. M.; Dada, A. O.; Pal, U., In Situ Growth Facilitated Photocharge Dynamics in ZIF-8- and NiS-Decorated ZnO Nanorods for Enhanced H2 Production. ACS Applied Nano Materials **2025**,8,3312-3322

2. Jaksani, B.; Gonuguntla, S.; Islam, H.; Pal, U., Heterostructures, Plasmonics, and Quantum Dot Photocatalysts for Hydrogen Production. In *Advances in Photocatalysis, Electrocatalysis and Photoelectrocatalysis for Hydrogen Production*, Balakrishna, R. G.; Shwetharani, R.; Jayaraman, T., Eds. RSC: 2024; 47, 222 - 243.

3. Sutar, D. N.; Pramod, A. K.; Islam, H.; Sesha Sainath, A. V.; Pal, U.; Batabyal, S. K., Cs3Bi2Cl3Br6:g-C3N4 Nanostructure-Based Thin Film Photocatalysts for Hydrogen Production under Daylight and Simulated Light. *ACS Applied Nano Materials* **2024,** *7* (22), 25556-25568.

4. Sk, S.; Islam, H.; Abraham, B. M.; Mondal, I.; Pal, U., Defects in MOFs for Photocatalytic Water Reduction to Hydrogen Generation: From Fundamental Understanding to State-of-Art Materials. *Small Methods 2024, 2401689*.

5. Kshirsagar, S. D.; Shelake, S. P.; Islam, H.; Bhattacharyya, S.; Ahmadipour, M.; Sesha Sainath, A. V.; Pal, U., In situ decoration of Cd0.05Mn0.05Zn0.90 (ZIF-8) photocatalyst for solar-driven hydrogen production. *Int. J. Hydrogen Energy.137 (2025) 1260–1268*

6. Fu, J.; Dong, J.; Si, R.; Sun, K.; Zhang, J.; Li, M.; Yu, N.; Zhang, B.; Humphrey, M. G.; Fu, Q.; Huang, J., Synergistic Effects for Enhanced Catalysis in a Dual Single-Atom Catalyst. *ACS Catalysis* **2021,** *11* (4), 1952-1961.

7. Xie, W.; Liu, Y.; Zhang, X.; Yan, H.; Liu, X. H.; Zhang, X.; Zhao, Q.; Huang, H. J. A. C., Asymmetric Cu− N− La Species Enabling Atomic-Level Donor-Acceptor Structure and Favored Reaction Thermodynamics for Selective CO2 Photoreduction to CH4. Angew. Chem. Int. Ed. 2024, 63, e202314384

8. Li, H.; Li, R.; Liu, G.; Zhai, M.; Yu, J., Noble-Metal-Free Single- and Dual-Atom Catalysts for Artificial Photosynthesis. Adv. Mater. 2024, 36, 2301307.

9. Lazaar, N.; Wu, S.; Qin, S.; Hamrouni, A.; Bikash Sarma, B.; Doronkin, D. E.; Denisov, N.; Lachheb, H.; Schmuki, P., Single-Atom Catalysts on C3N4: Minimizing Single Atom Pt Loading for Maximized Photocatalytic Hydrogen Production Efficiency. Angew. Chem. Int. Ed. 2025, 64, e202416453

10. Zhang, W.; Chao, Y.; Zhang, W.; Zhou, J.; Lv, F.; Wang, K.; Lin, F.; Luo, H.; Li, J.; Tong, M.; Wang, E.; Guo, S., Emerging Dual-Atomic-Site Catalysts for Efficient Energy Catalysis. Adv. Mater. 2021, 33, 2102576

11. Mo, S.; Zhao, X.; Li, S.; Huang, L.; Zhao, X.; Ren, Q.; Zhang, M.; Peng, R.; Zhang, Y.; Zhou, X. J. A. C. I. E., Non-Interacting Ni and Fe Dual-Atom Pair Sites in N-Doped Carbon Catalysts for Efficient Concentrating Solar-Driven Photothermal CO2 Reduction. Angew. Chem. Int. Ed. 2023, 62, e202313868

12. Liu, Y.; Sun, Y.; Zhao, E.; Yang, W.; Lin, J.; Zhong, Q.; Qi, H.; Deng, A.; Yang, S.; Zhang, H.; He, H.; Liu, S.; Chen, Z.; Wang, S., Atomically Dispersed Silver-Cobalt Dual-Metal Sites Synergistically Promoting Photocatalytic Hydrogen Evolution. Adv. Funct. Mater. 2023, 33, 2301840

13. Li, Y.; Luan, D.; Lou, X. W., Engineering of Single-Atomic Sites for Electro- and Photo-Catalytic H2O2 Production. Adv. Mater. 2024, 36, 2412386

14. Lian, Z.; Gao, F.; Xiao, H.; Luo, D.; Li, M.; Fang, D.; Yang, Y.; Zi, J.; Li, H. J. A. C. I. E., Photo-self-Fenton Reaction Mediated by Atomically Dispersed Ag− Co Photocatalysts toward Efficient Degradation of Organic Pollutants. Angew. Chem. Int. Ed.**2024,** *63* (8), e202318927.

15. Wang, Y.-F.; Qi, M.-Y.; Conte, M.; Tang, Z.-R.; Xu, Y.-J., Bimetallic Single Atom/Nanoparticle Ensemble for Efficient Photochemical Cascade Synthesis of Ethylene from Methane. Angew. Chem. Int. Ed. 2024, 63, e202407791.
16. Wang, A.; Li, J.; Zhang, T. J. N. R. C., Heterogeneous single-atom catalysis.Nature Reviews chemistry. **2018,** *2* (6), 65-81.
17. Yan, H.; Cheng, H.; Yi, H.; Lin, Y.; Yao, T.; Wang, C.; Li, J.; Wei, S.; Lu, J. J. J. o. t. A. c. s., Single-atom Pd1/graphene catalyst achieved by atomic layer deposition: remarkable performance in selective hydrogenation of 1, 3-butadiene. Am. Chem. Soc. 2015, 137, 10484−10487
18. Xiao, M.; Zhu, J.; Li, G.; Li, N.; Li, S.; Cano, Z. P.; Ma, L.; Cui, P.; Xu, P.; Jiang, G. J. A. C. I. E., A single-atom iridium heterogeneous catalyst in oxygen reduction reaction. Angew. Chem. Int. Ed. **2019,** *58* (28), 9640-9645.
19. Li, J.; Chen, S.; Yang, N.; Deng, M.; Ibraheem, S.; Deng, J.; Li, J.; Li, L.; Wei, Z. J. A. C., Ultrahigh-loading zinc single-atom catalyst for highly efficient oxygen reduction in both acidic and alkaline media. Angew. Chem. Int. Ed. **2019,** *131* (21), 7109-7113.
20. Ren, Y.; Tang, Y.; Zhang, L.; Liu, X.; Li, L.; Miao, S.; Sheng Su, D.; Wang, A.; Li, J.; Zhang, T. J. N. c., Unraveling the coordination structure-performance relationship in Pt1/Fe2O3 single-atom catalyst. Nature Communication. **2019,** *10* (1), 4500.
21. Varangane, S.; Madhu, R.; Mehmood, S.; Jaksani, B.; Bhasin, V.; Abraham, B. M.; Nagaraj, A.; Vennapoosa, C. S.; Reddy, B. S.; Kundu, S. J. J. o. M. C. A., Atomically dispersed Ru sites on MOF-derived NC-ZnO for efficient oxygen evolution reaction in acid media. J. Mater. Chem. A **2024,** *12* (21), 12533-12544.
22. Chen, F.; Yang, Q.; Wang, Y.; Zhao, J.; Wang, D.; Li, X.; Guo, Z.; Wang, H.; Deng, Y.; Niu, C. J. A. C. B. E., Novel ternary heterojunction photcocatalyst of Ag nanoparticles and g-C3N4 nanosheets co-modified BiVO4 for wider spectrum visible-light photocatalytic degradation of refractory pollutant. Applied Catalysis B: Environmental 205 (2017) 133–147.
23. Chen, F.; Liu, L. L.; Wu, J. H.; Rui, X. H.; Chen, J. J.; Yu, Y. J. A. M., Single-atom iron anchored tubular g-C3N4 catalysts for ultrafast fenton-like reaction: roles of high-valency iron-oxo species and organic radicals. Adv. Mater. **2022,** *34* (31), 2202891.
24. Liu, Y.; Sun, Y.; Zhao, E.; Yang, W.; Lin, J.; Zhong, Q.; Qi, H.; Deng, A.; Yang, S.; Zhang, H. J. A. F. M., Atomically dispersed silver-cobalt dual-metal sites synergistically promoting photocatalytic hydrogen evolution. Adv. Funct. Mater. 2023, 33, 2301840**.**

25. Lian, Z.; Gao, F.; Xiao, H.; Luo, D.; Li, M.; Fang, D.; Yang, Y.; Zi, J.; Li, H., Photo-self-Fenton Reaction Mediated by Atomically Dispersed Ag−Co Photocatalysts toward Efficient Degradation of Organic Pollutants. Angew. Chem. Int. Ed.**2024,** *63* (8), e202318927.
26.Bi, G.; Ding, R.; Song, J.; Luo, M.; Zhang, H.; Liu, M.; Huang, D.; Mu, Y. J. A. C., Discriminating the Active Ru Species Towards the Selective Generation of Singlet Oxygen from Peroxymonosulfate: Nanoparticles Surpass Single-Atom Catalysts. Nano Energy 61 (2019) 245-250.
27. Su, L.; Wang, P.; Ma, X.; Wang, J.; Zhan, S. J. A. C., Regulating local electron density of iron single sites by introducing nitrogen vacancies for efficient photo-fenton process. Angew. Chem. Int. Ed**. 2021,** *133* (39), 21431-21436.
28. Sarma, B. B.; Maurer, F.; Doronkin, D. E.; Grunwaldt, J.-D., Design of Single-Atom Catalysts and Tracking Their Fate Using Operando and Advanced X-ray Spectroscopic Tools. *Chemical Reviews* **2023,** *123* (1), 379-444.
29. Timoshenko, J.; Kuzmin, A.; Purans, J. J. J. o. P. C. M., EXAFS study of hydrogen intercalation into ReO 3 using the evolutionary algorithm. J. Phys.: Condens. Matter. **2014,** *26* (5), 055401.
30. He, T.; Zhang, C.; Zhang, L.; Du, A. J. N. R., Single Pt atom decorated graphitic carbon nitride as an efficient photocatalyst for the hydrogenation of nitrobenzene into aniline. Nano Research. 2019, *12*, 1817-1823.
31. Zhang, H.; Tian, W.; Duan, X.; Sun, H.; Liu, S.; Wang, S. J. A. M., Catalysis of a single transition metal site for water oxidation: from mononuclear molecules to single atoms. *Int. J. Hydrogen Energy.* **2020,** *32* (18), 1904037.
32. Zhou, T.; Wei, H.; Xiao, B.; Lv, T.; Duan, L.; Lu, Q.; Zhang, J.; Zhang, Y.; Liu, Q. J. R. a., Anchored Cu single atoms on porous gC 3 N 4 for superior photocatalytic H 2 evolution from water splitting. *RSC Adv. 2023, 13 (13), 8915-8922.*
33. Mo, S.; Zhao, X.; Li, S.; Huang, L.; Zhao, X.; Ren, Q.; Zhang, M.; Peng, R.; Zhang, Y.; Zhou, X.; Fan, Y.; Xie, Q.; Guo, Y.; Ye, D.; Chen, Y., Non-Interacting Ni and Fe Dual-Atom Pair Sites in N-Doped Carbon Catalysts for Efficient Concentrating Solar-Driven Photothermal CO2 Reduction. Angew. Chem. Int. Ed. 2023, 62, e202313868.
34. Shao, W.; Yu, M.; Xu, X.; Han, X.; Chen, Y.; Han, J.; Wu, G.; Xing, W. J. S., Design of a Single-Atom In–N3–S site to Modulate Exciton Behavior in Carbon Nitride for Enhanced Photocatalytic Performance. Small,2024, *20* (24), 2306567.

35. Kalita, S. J.; Varangane, S.; Basyach, P.; Sonowal, K.; Abraham, B. M.; Guha, A. K.; Pal, U.; Saikia, L., InVO4-Decorated Ti3C2 MXene for Efficient Photocatalytic Hydrogen Evolution. *ACS Applied Materials & Interfaces* **2024,** *16* (31), 40825-40835.
36. Hu, J.; Liu, H.; Hu, C.; Jiao, F. J. A. S. S., Insights from DFT and mechanistic analysis of surface-precision carbon self-doped porous g-C3N4 for enhanced visible light-driven hydrogen evolution. Applied Surface Science 670 (2024) 160679.
37. Zhang, X.; Zhang, X. R.; Yang, P.; Chen, H.-S. J. C. E. J., Black magnetic Cu-g-C3N4 nanosheets towards efficient photocatalytic H2 generation and CO2/benzene conversion. *Chem. Eng. J.* **2022,** *450*, 138030.
38. Ismael, M. J. I. C. C., One-step ultrasonic-assisted synthesis of Ni-doped g-C3N4 photocatalyst for enhanced photocatalytic hydrogen evolution. Inorganic Chemistry Communications 151 (2023) 110607.
39. Zhou, Y.; Lv, W.; Zhu, B.; Tong, F.; Pan, J.; Bai, J.; Zhou, Q.; Qin, H. J. A. S. C.; Engineering, Template-free one-step synthesis of g-C3N4 nanosheets with simultaneous porous network and S-doping for remarkable visible-light-driven hydrogen evolution. ACS Sustainable Chem. Eng. 2019, 7, 5801−5807
40. Liu, Y.; Zhang, Z.; Zhang, L.; Xia, Y.; Wang, H.; Liu, H.; Ge, S.; Yu, J. J. J. o. M. C. A., Manipulating the d-band centers of transition metal phosphides through dual metal doping towards robust overall water splitting. J. Mater. Chem. A**. 2022,** *10* (41), 22125-22134.
41. Jin, Z.; Zhang, L. J. J. o. M. S.; Technology, Performance of Ni-Cu bimetallic co-catalyst g-C3N4 nanosheets for improving hydrogen evolution. Journal of Materials Science & Technology 49 (2020) 144–156.
42. Du, C.; Feng, J.; Xu, S.; Pang, B.; Dong, H.; Yu, L.; Dong, L. J. I. J. o. H. E., Enhancing photocatalytic hydrogen evolution of g-C3N4 via oxygen-containing groups. *Int. J. Hydrogen Energy* **2024,** *53*, 280-289.
43. Gujjula, S. R.; Pal, U.; Chanda, N.; Karingula, S.; Chirra, S.; Siliveri, S.; Goskula, S.; Narayanan, V. J. E.; Fuels, Versatile bifunctional Ag@ g-C3N4/r-GO catalyst for efficient photo-and electrocatalytic H2 production. Energy Fuels. **2023,** *37* (13), 9722-9735.
44. Zhou, G.; Zhang, L.; Xia, Y.; Yin, W.; Zhu, X.; Hou, J.; Wang, S.; Ning, X.; Wang, X. J. J. o. C. P., Remarkably enhanced hydrogen evolution of g-C3N4 nanosheet under simulated sunlight via AgPt alloy co-catalyst with low amount of Pt. Journal of Cleaner Production 434 (2024) 139950.

45. Sun, Y.; Hao, Y.; Lin, X.; Liu, Z.; Sun, H.; Jia, S.; Chen, Y.; Yan, Y.; Li, X., Efficient electron transport by 1D CuZnInS modified 2D Ti3C2 MXene for enhanced photocatalytic hydrogen production. *Journal of Colloid and Interface Science* **2024,** *653*, 396-404.

TOC